Carrier Dynamics in Highly Quantum-Confined, Colloidal Indium Antimonide Nanocrystals

Angela Y. Chang,[†] Wenyong Liu,[‡] Dmitri V. Talapin,[‡,§] and Richard D. Schaller[†,§,*]

[†]Department of Chemistry, Northwestern University, Evanston, Illinois 60208, United States, [‡]Department of Chemistry and James Franck Institute, University of Chicago, Chicago, Illinois 60637, United States, and [§]Center for Nanoscale Materials, Argonne National Laboratory, Argonne, Illinois 60439, United States

ABSTRACT Nanometer-sized particles of indium antimonide (InSb) offer opportunities in areas such as solar energy conversion and single photon sources. Here, we measure electron–hole pair dynamics, spectra, and absorption cross sections of strongly quantum-confined colloidal InSb nanocrystal quantum dots using femtosecond transient absorption. For all samples, we observe a bleach feature that develops on ultrafast time scales, which notably moves to lower energy during the first several picoseconds following excitation. We associate this unusual red shift, which becomes larger for larger particles and more distinct at lower sample temperatures, with hot exciton cooling through states that we suggest arise from energetically proximal conduction band levels. From controlled optical excitation intensities, we determine biexciton lifetimes, which range from 2 to 20 ps for the studied 3–6 nm diameter particle sizes.

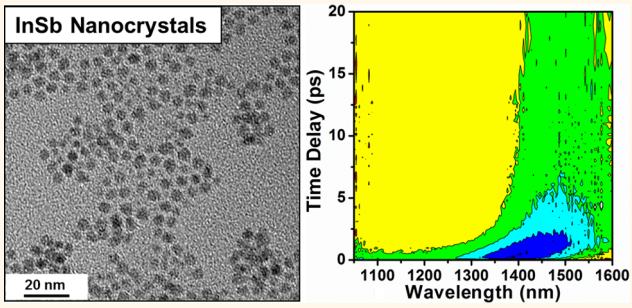

KEYWORDS: indium antimonide · InSb · semiconductor nanocrystals · nanocrystal quantum dots · transient absorption · Auger recombination · intraband relaxation

Due to size-tunable absorption and photoluminescence (PL), colloidally prepared semiconductor nanocrystals (NCs) have attracted significant interest for use as biolabels,[1] optical amplifiers,[2,3] photodetectors,[4,5] light-emitting diodes,[6–8] and single photon sources.[9] In particular, NCs derived from narrow band gap bulk-phase semiconductors are appealing for use in solar cells both because the size-tunable energy gap (E_g) facilitates maximal single junction power conversion efficiency,[10–13] and quantum confinement promotes useful physical phenomena, including the low threshold formation of multiple electron–hole pairs (excitons) per absorbed photon, which can potentially improve energy extraction from blue solar photons.[14–16] Compared to other narrow gap semiconductors such as PbSe,[17,18] Ge,[19,20] and HgTe,[21,22] InSb remains unexamined owing to difficulties related to the synthesis of this composition by wet chemical techniques, which limited previous studies of this composition to epitaxially prepared quantum dots.[23–25] Such epitaxial InSb dots reportedly interacted electronically with synthetically required substrates, thereby preventing strong quantum confinement.[26,27] Recently developed synthetic routes to colloidal InSb NCs[28–30] now permit examination of this composition under the influence of a highly confining potential.

To understand the behavior of 3D quantum-confined InSb, we consider bulk-phase properties. Bulk zinc-blende InSb exhibits a small direct band gap of 0.17 eV at 300 K (0.235 eV at 2 K)[31] and a large exciton Bohr radius of ~60 nm,[32,33] such that excitons generated in few-nanometer NCs, as studied here, experience particularly strong quantum confinement. Given that the Γ-valley effective masses of the electron and hole are $0.014m_0$ and $0.43m_0$ (m_0 is the electron rest mass), respectively,[31] quantum confinement is expected to predominantly discretize and shift electron energy levels. In contrast, hole states retain bulk-like band structure for diameters larger than 3 nm.[32] Additionally, bulk InSb presents heavier electron effective masses in the L- and X-valleys (at 0.68 and 1.0 eV, respectively) compared to that in the Γ-valley. As a result,

* Address correspondence to schaller@anl.gov, schaller@northwestern.edu.

Received for review June 10, 2014 and accepted August 8, 2014.

Published online August 08, 2014
10.1021/nn5031274

© 2014 American Chemical Society

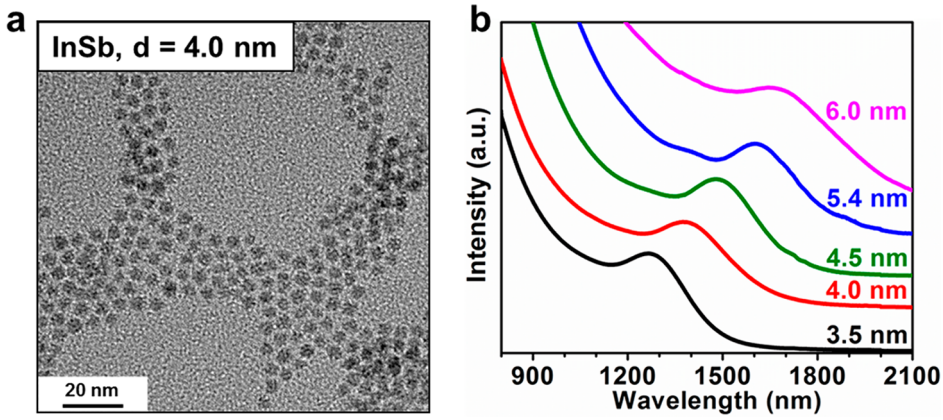

Figure 1. (a) TEM image of colloidal InSb NCs 4.0 nm in diameter. (b) Absorption spectra of colloidal InSb NCs for a range of sizes.

theoretical studies have predicted that, for sufficiently small InSb particles, the L-valley can become the lowest-energy transition and impart indirect band-edge character.[34]

Here, we perform optical characterizations of colloidal InSb NCs, including transient absorption (TA) spectra, dynamics, and absorption cross-section measurements for multiple NC sizes. Immediately following low fluence excitation, we observe the formation of a near-infrared (NIR) bleach feature in proximity to the static absorption maximum that, for several picoseconds, dramatically red shifts prior to reaching a time-independent position. We suggest that this unusual bleach shift, which does not appear for InAs NCs, relates transient population flow through two energetically proximal absorbing states originating from the Γ-valley and either the L- or X-valley. This time-dependent spectral shift persists at low temperatures and obeys Varshni relations (dE_g/dT) in similarity to bulk InSb, suggesting an intrinsic origin. Picosecond formation times of the lowest-energy bleach as well as slower intraband cooling for larger NC sizes suggests Auger electron-to-hole energy transfer from widely spaced electron levels to more dense hole states. Lastly, we determine absorption cross sections for multiple sizes *via* pump-fluence-dependent measurements, show that InSb NCs undergo rapid biexcitonic Auger recombination, and determine the biexciton lifetime as a function of particle size.

RESULTS AND DISCUSSION

Figure 1a presents a transmission electron microscopy (TEM) image of highly monodisperse, approximately spherical, 4.0 nm diameter InSb NCs (additional sizes appear in Supporting Information, Figure S1). Absorption spectra of the particles examined in this work, shown in Figure 1b, exhibit a distinct absorption onset and peak in the NIR spectral range that shifts to lower energy with increasing particle size, as is typical of electronic quantum confinement. The absorption spectra at higher energies appear fairly featureless and lack prominent additional peaks, which prevents evaluation of electronic level ordering. For a given InSb NC size, the line width of the lowest-energy absorption feature was typically ~180 meV (estimated using twice the half-width at half-maximum). Using experimentally derived particle sizes and lowest-energy absorption feature maxima, we produced an empirical InSb sizing curve:

$$D = 125.5 - 376.3E + 393.0E^2 - 138.8E^3 \quad (1)$$

where D is NC diameter (in nm) and E is the lowest-energy absorption feature maximum (in eV).

A spectrally resolved transient absorption map and several time-delayed TA spectra for 4.0 nm diameter InSb NCs at 298 K are shown in Figure 2a,b, respectively. Following 800 nm excitation using a sufficiently low fluence such that exclusively single excitons are produced in excited NCs (average number of excitons per NC, $\langle N \rangle = 0.09$, determination of which is discussed below), we observe instrument-limited (~60 fs) formation of a bleach feature (negative differential absorption) near 1400 nm. Notably, the initial bleach center-of-mass undergoes a clear shift to lower energy within the first several picoseconds following excitation and stabilizes near 1510 nm (Figure 2c). Such red shifting occurs in TA spectra for all InSb NCs examined in this work. For comparison, and to rule out potential artifacts, we performed TA measurements on 4.9 nm InAs NCs and show that for this composition the bleach feature does not exhibit comparable shifting (Figure S2).

Examination of InSb NC dynamics at the positions of the early and late-time bleach maxima shows a rapid initial decay near 1400 nm as well as a delayed rise near 1510 nm (Figure 3a), followed by decay of the 1510 nm bleach on longer time scales (Figure 3a inset). In particular, the delayed rise suggests intraband relaxation as the origin of the bleach red shift. To further establish the intraband relaxation origin, we examined bleach formation dynamics for an InSb NC sample following excitation at multiple excitation wavelengths. Such measurements yield more rapid bleach formation with

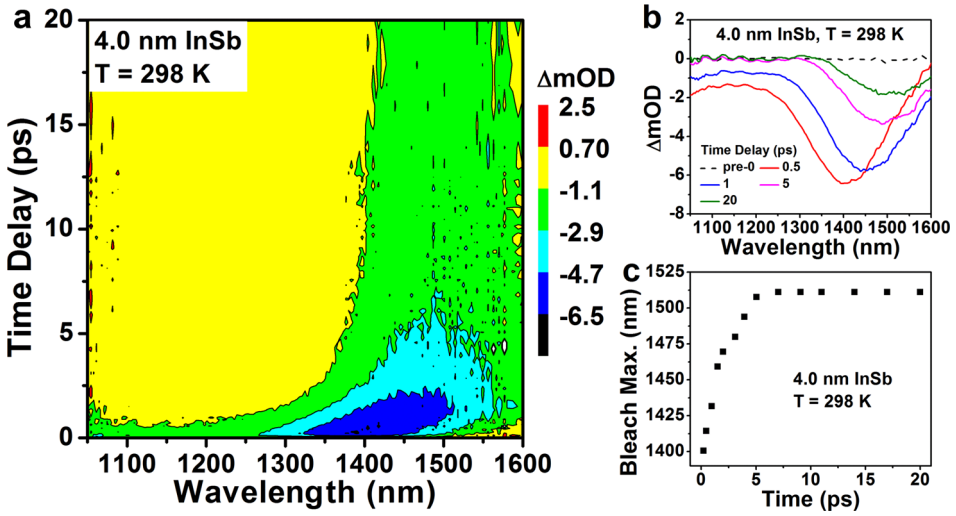

Figure 2. TA spectra and dynamics at 298 K. (a) Multispectral, time-resolved plot and (b) several time-delayed TA spectra obtained for 4.0 nm InSb NCs excited at 800 nm ($\langle N \rangle = 0.09$) show a shift in the bleach center-of-mass with pump−probe delay time. (c) Plot of the location of the bleach maximum *versus* time delay for 4.0 nm InSb. The observed bleach maximum shifts by ~65 meV.

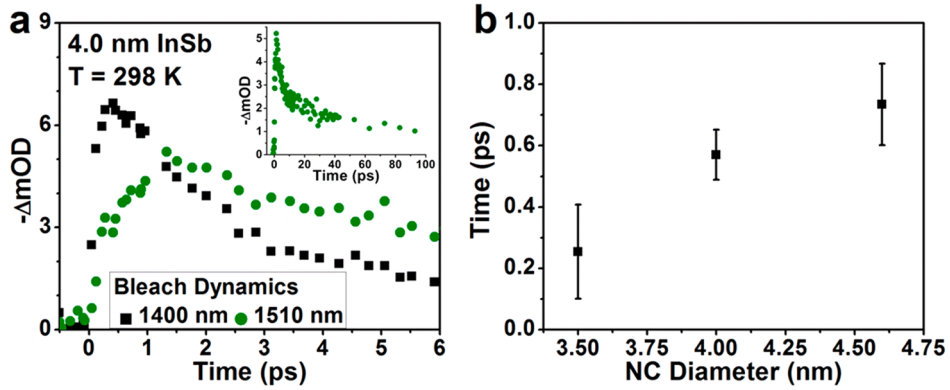

Figure 3. (a) Bleach dynamics of 4.0 nm InSb NCs at probe wavelengths of 1400 and 1510 nm at 298 K. The delayed rise near 1510 nm suggests intraband relaxation as the origin of the bleach red shift. The inset depicts the 1510 nm bleach out to 100 ps. (b) Intraband relaxation times for multiple particle sizes.

reduction of the pump photon energy (Figure S3), in accord with expected hot carrier cooling trends. As a function of NC size, intraband relaxation times become slower with increasing particle size (Figure 3b), which suggests confinement-enhanced electron-to-hole Auger energy transfer relaxation, as has been observed in other NC compositions.[35−39] We obtained intraband relaxation time constants of 0.25 ± 0.15, 0.57 ± 0.08, and 0.73 ± 0.13 ps for InSb NCs of 3.5, 4.0, and 4.5 nm in diameter, respectively. The 1510 nm bleach decays on a time scale of 31 ± 3 ps at room temperature. Single exciton dynamics measured in multiple samples exhibited bleach decay times that lacked systematic behavior, which suggests involvement of an extrinsic process such as electron trapping at defects, likely in association with the NC−ligand interface.

Regarding the origin of the unusual bleach red shift, we consider numerous aspects. In all, the observed bleach maximum shifts by ~65 meV for 4.0 nm InSb (Figure 2c), which exceeds any available phonon energy in InSb. Also, the rate of red shift far exceeds interparticle energy transfer rates by at least 2 orders of magnitude.[40] Furthermore, it is important to notice that the bleach line width remains fairly constant throughout the relaxation process, which suggests transfer of population between distinct, yet similarly broadened, electronic states. As shown in Figure S4, the initial and final bleach positions exist within the bandwidth of the static absorption feature, consistent with a state-filling origin rather than a stimulated emission process. Moreover, Table S1 shows that this red shift magnitude *decreases* for decreasing particle size, with shifts of 71, 65, and 56 meV (error for these values is estimated to be 5−10%) for 4.3, 4.0, and 3.5 nm NCs, respectively. This trend differs from the tendency of different angular momentum envelope wave functions originating from the same valley to become more widely spaced with increasing quantum

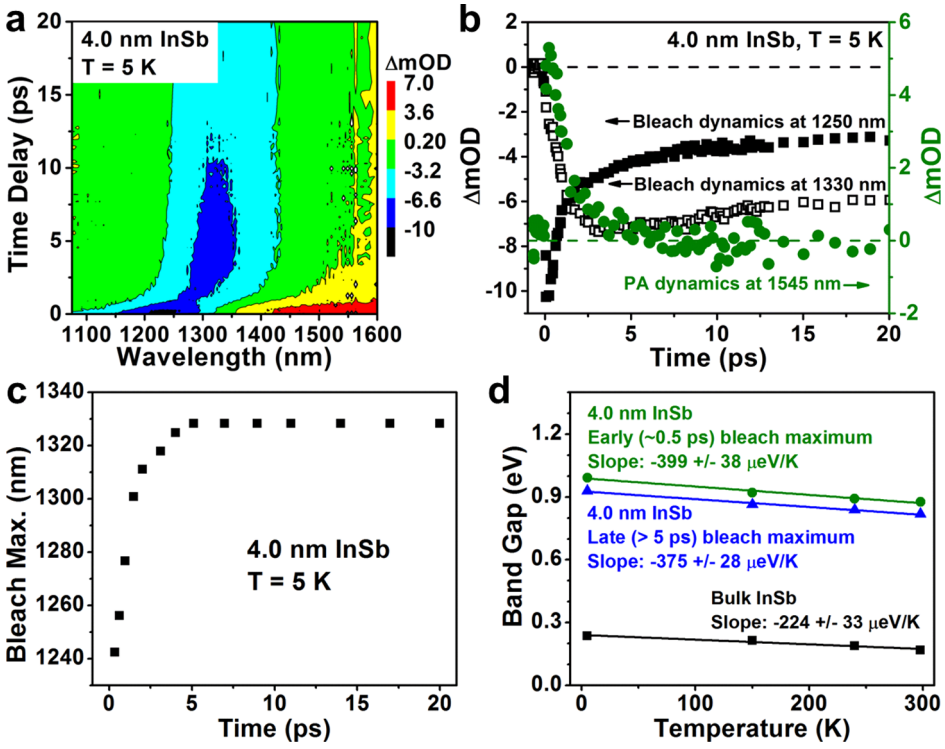

Figure 4. Low-temperature TA spectra and dynamics for 4.0 nm InSb NCs. (a) Multispectral, time-resolved TA plot shows that the bleach and bleach shift occur at higher energies at 5 K than at 298 K. (b) Dynamics at 5 K ($\langle N \rangle = 0.11$) for the initial (solid black squares) and final bleach positions (open black squares) near 1250 and 1330 nm, respectively, and the PA (green solid circles, monitored at 1545 nm). Arrows point to the corresponding *y*-axis for the data points. (c) Time dependence of the bleach maximum, which shows a ~65 meV shift. (d) Plot of early and late bleach positions *versus* sample temperature for 4.0 nm NCs and bulk InSb reflect the Varshni dependence.

confinement. Instead, we suggest that the origin of the bleach shift involves multiple conduction band valleys of InSb, which exhibit important differences from those of InAs. The L- and X-valleys for bulk InAs appear at 1.08 and 1.37 eV, respectively, which precludes energetic proximity to the Γ-valley upon quantum confinement for the energy gap range examined. In contrast, for InSb, the electron effective masses in the L- and X-valleys exceed that in the Γ-valley such that quantum-confined states produced from such higher-energy valleys can become energetically proximal[34] and coupled[41] to Γ-valley-derived transitions. Furthermore, such coupling is expected to increase as roughly the square root of the percentage of the NC band gap produced by quantum confinement,[41] which in 3−6 nm InSb NCs is particularly large. Such a band-coupling effect, thus, appears as a reasonable interpretation of the observed trends, and therefore, we propose that the bleach shift relates transient population flow through two energetically proximal absorbing states derived from the Γ-valley and either the L- or the X-valley.

TA measurements performed on 4.0 nm InSb at reduced sample temperatures are shown in Figure 4. The multispectral TA plot (Figure 4a) exhibits a similar bleach red shift at 5 K compared to that observed at 298 K, though at a higher energy. A photoinduced absorption (PA) feature at low energies is also observed, which decays in step with the bleach decay dynamics as monitored near 1250 nm, the position of the initial bleach maximum (Figure 4b; the final bleach position is near 1330 nm). Here, the respective PA and bleach decay lifetimes are 1.32 ± 0.12 and 1.34 ± 0.09 ps. We note that this decay time does not substantially change from that observed in 298 K data and again reflects intraband relaxation dynamics (see also Figure S5 for a direct comparison of 5 and 298 K dynamics). As the PA feature lacks a discernible peak (Figure S6), increased oscillator strength of hot carriers seems a likely origin, rather than a prominent carrier-induced Stark effect (which typically would produce a distinct PA peak).[39,42] Figure 4c shows that the energy difference between the initial and final bleach at low temperature remains at ~65 meV, which is indistinguishable from the room temperature observation. Figure 4d indicates the position of the early and late bleach for additional intermediate temperature TA data, the bulk-phase Varshni energy gap dependence on temperature, and linear fits to the data points to obtain dE_g/dT. Obtained slopes exhibit the same sign and differ by less than a factor of 2. The comparable dependence on temperature of both the early and late bleach to the bulk trend suggests that these features arise from the inherent InSb electronic structure.

Next, we examined the optical response of InSb NCs as a function of pump fluence. Figure 5 displays pump-power-dependent bleach amplitudes of 4.5 nm InSb NCs for several pump−probe time delays. At lower pump intensities, the bleach amplitudes at both early and late time delays exhibit proportionate scaling with intensity. At higher pump intensities, the late-time bleach amplitude exhibits saturation (becomes sublinear), while the early-time bleach displays saturation only at still higher fluences. Such saturation behavior is typical for 3D-confined semiconductor NCs and is attributed to state filling of the lowest-energy conduction band state according to the band-edge exciton degeneracy (here two-fold degenerate). Multiexciton Auger recombination is well-known to produce the differences in early to late bleach amplitude since the process yields single excitons in all excited NCs for delay times sufficiently in excess of the Auger recombination time.[42] Thus, the difference in amplitude between early (black squares) and late (blue triangles) bleach signals suggests the presence of this annihilation process. Because only single excitons remain at times significantly in excess of the Auger recombination lifetime, the NC absorption cross section (σ) for a given pump wavelength is obtained from the bleach amplitude (A) using

$$A(j, \lambda_{pump}) = B(1 - e^{-\sigma j}) \quad (2)$$

where j is the pump photon fluence and B is a bleach amplitude scaling factor.[43] Absorption cross sections for several NC sizes, summarized in Table 1, were obtained by fitting eq 2 to data from pump-power-dependent TA measurements. We estimated the absorption cross sections of InSb NCs at 800 nm using the local field correction approach that has been successful for other semiconductor NC compositions.[42,44] Specifically, we utilize

$$\sigma_{800nm} = (n_{bulk}/n_s)\alpha_{bulk} V |f|^2 \quad (3)$$

where α_{bulk} and n_{bulk} are the absorption coefficient and refractive index of the bulk semiconductor, respectively; n_s is the solvent refractive index (here the solvent is tetrachloroethylene); V is the NC volume; and f is the local field factor that accounts for the difference in the electric field inside and outside of the NC. Using optical constants for bulk InSb,[45] we estimate $\sigma_{800nm}(cm^2) = 1.01 \times 10^{-16}[R(nm)]^3$, where R is the NC radius. The experimental cross sections trend similarly to calculated values, with the measured values up to two times greater than calculation for all NC sizes examined, suggesting a small but systematic deviation in either pump fluence determination, accuracy of the calculation inputs, or applicability of bulk material calculation inputs for such a highly quantum-confined material.

We further investigated the power-dependent dynamics of the InSb NCs in order to characterize

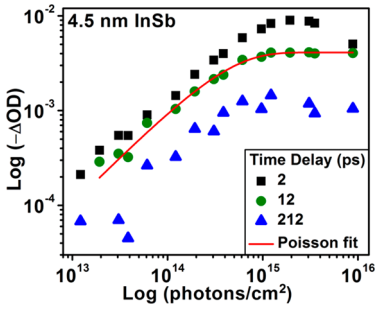

Figure 5. Pump-power-dependent measurements of 4.5 nm InSb shown at 2, 12, and 212 ps time delays. To obtain absorption cross-section values, a Poisson function that assumes only single exciton occupancy (red line) was fit through traces that showed signal saturation at high fluence for time delays in excess of Auger recombination lifetimes.

TABLE 1. Calculated and Measured Absorption Cross-Section Values for InSb NC Samples

InSb NC diameter (nm)	calculated cross section (10^{-16} cm^2)	measured cross section (10^{-16} cm^2)
3.5	5.41	7.05 ± 1.23
4.0	8.07	15.3 ± 1.18
4.5	11.5	25.3 ± 1.09
5.4	19.9	45.7 ± 3.08
6.0	27.2	35.9 ± 11.0

biexciton lifetimes. Figure 6a depicts bleach recovery dynamics for 6.0 nm InSb NCs, which are shown normalized by values at long delay time. At two different low pump powers ($\langle N \rangle$ = 0.15 and 0.32), the TA traces decay with time due to carrier trapping but otherwise appear indistinguishable because primarily only unexcited or singly excited NCs exist at these fluences. At higher pump powers ($\langle N \rangle$ = 0.87 and 2.07), we clearly observe faster features emerging in the dynamics, consistent with biexciton and higher-order exciton Auger recombination.[42,46] To determine biexciton lifetimes as a function of NC size, we subtracted the low fluence signal, normalized at long time, from similarly normalized higher fluence signals, for which the ensemble described by $\langle N \rangle$ should contain a biexciton population component according to Poisson statistics. We fit the resulting difference with a mono-exponential decay function (Figure 6a inset) and obtained time constants of 2.40 ± 0.36, 6.34 ± 1.90, and 16.7 ± 5.90 ps for 4.0, 4.5, and 5.4 nm InSb, respectively. In Figure 6b, the biexciton lifetimes are plotted as a function of NC volume. The biexciton lifetimes for these InSb NCs scale linearly with NC volume, consistent with the Auger recombination behavior observed in other semiconductor nanocrystals.[39,42,47] We note that these InSb NCs exhibit faster biexciton decay compared to those reported for PbSe NCs;[48] however, these values are comparable to biexciton lifetimes determined for InAs NCs.[39] Such fast Auger recombination could

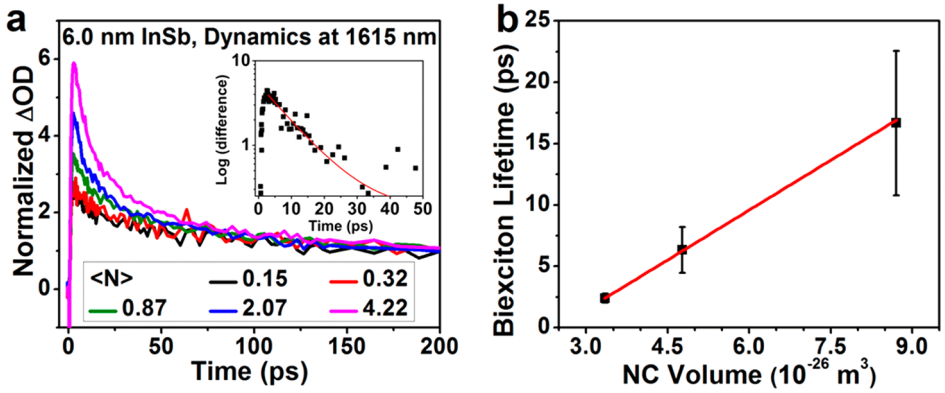

Figure 6. (a) Power-dependent bleach dynamics of 6.0 nm InSb NCs normalized by the signal at long delay times. For shown traces, the average NC occupancy $\langle N \rangle$ is 0.15 (black), 0.32 (red), 0.87 (green), 2.07 (blue), and 4.22 (pink). As $\langle N \rangle$ increases, a fast feature clearly emerges, which is attributed to multiexciton annihilation. The inset shows the difference between high and low intensity normalized traces as well as a single exponential fit to the data, from which the biexciton lifetime is derived. (b) Biexciton lifetimes, plotted as a function of InSb NC volume (in m^3), exhibit a linear increase with particle volume.

present challenges for using InSb in optical amplifiers;[3] however, the rapidity of its multiexciton annihilation could benefit applications such as single photon emitters.

CONCLUSIONS

In conclusion, we optically characterized colloidally prepared InSb NCs ranging from 3 to 6 nm in diameter. In TA spectra, we observed an unusual bleach red shift. Given the magnitude of this red shift and the related dynamics, we suggest that the bleach red shift arises from transfer of population between two optical transitions of comparable energy within a manifold involving multiple coupled conduction band states. Further, we investigated carrier dynamics as a function of pump power, from which we derived values for the experimental absorption cross sections and biexciton lifetimes.

METHODS

Zinc-blende colloidal InSb NCs, with average sizes between 3 and 6 nm in diameter and passivated with oleylamine and oleic acid ligands, were synthesized as reported previously.[28] For measurements performed at room temperature (298 K), all samples were suspended in tetrachloroethylene, loaded into an airtight 1 mm quartz cuvette under a nitrogen environment, and continuously stirred. For comparison, we examined samples of InAs NCs, which were synthesized according to published methods.[49] For measurements performed at lower temperatures, InSb NCs were prepared as a dry film under a nitrogen environment and loaded into an evacuated helium cryostat. TA measurements were performed using a 35 fs pulse width, 2 kHz commercial amplified Ti:sapphire laser operating at 800 nm. A portion (5%) of the amplifier output was time-delayed and then focused into a sapphire plate to produce a NIR white light probe. Except where indicated, the pump wavelength was 800 nm (1.55 eV), and the pump fluence was controllably varied from 0.005 to 2 mJ/cm^2.

Conflict of Interest: The authors declare no competing financial interest.

Acknowledgment. Use of the Center for Nanoscale Materials was supported by the U.S. Department of Energy, Office of Science, Office of Basic Energy Sciences under Contract No. DE-AC02-06CH11357. The work on the synthesis and characterization of InSb NCs was supported by NSF under Award Number DMR-1310398. D.V.T. also thanks the David and Lucile Packard Foundation and Keck Foundation. This work used facilities supported by NSF MRSEC Program under Award Number DMR 08-20054.

Supporting Information Available: Additional figures. This material is available free of charge *via* the Internet at http://pubs.acs.org.

REFERENCES AND NOTES

1. Kairdolf, B. A.; Smith, A. M.; Stokes, T. H.; Wang, M. D.; Young, A. N.; Nie, S. Semiconductor Quantum Dots for Bioimaging and Biodiagnostic Applications. *Annu. Rev. Anal. Chem.* **2013**, *6*, 143–162.
2. Klimov, V. I.; Mikhailovsky, A. A.; Xu, S.; Malko, A.; Hollingsworth, J. A.; Leatherdale, C. A.; Eisler, H.-J.; Bawendi, M. G. Optical Gain and Stimulated Emission in Nanocrystal Quantum Dots. *Science* **2000**, *290*, 314–317.
3. Kazes, M.; Lewis, D. Y.; Ebenstein, Y.; Mokari, T.; Banin, U. Lasing from Semiconductor Quantum Rods in a Cylindrical Microcavity. *Adv. Mater.* **2002**, *14*, 317–321.
4. Talapin, D. V.; Lee, J.-S.; Kovalenko, M. V.; Shevchenko, E. V. Prospects of Colloidal Nanocrystals for Electronic and Optoelectronic Applications. *Chem. Rev.* **2010**, *110*, 389–458.
5. McDonald, S. A.; Konstantatos, G.; Zhang, S.; Cyr, P. W.; Klem, E. J. D.; Levina, L.; Sargent, E. H. Solution-Processed PbS Quantum Dot Infrared Photodetectors and Photovoltaics. *Nat. Mater.* **2005**, *4*, 138–142.
6. Anikeeva, P. O.; Halpert, J. E.; Bawendi, M. G.; Bulović, V. Quantum Dot Light-Emitting Devices with Electroluminescence Tunable over the Entire Visible Spectrum. *Nano Lett.* **2009**, *9*, 2532–2536.
7. Kwak, J.; Bae, W. K.; Lee, D.; Park, I.; Lim, J.; Park, M.; Cho, H.; Woo, H.; Yoon, D. Y.; Char, K.; *et al.* Bright and Efficient Full-Color Colloidal Quantum Dot Light-Emitting Diodes Using an Inverted Device Structure. *Nano Lett.* **2012**, *12*, 2362–2366.
8. Sun, L.; Choi, J. J.; Stachnik, D.; Bartnik, A. C.; Hyun, B.-R.; Malliaras, G. G.; Hanrath, T.; Wise, F. W. Bright Infrared Quantum-Dot Light-Emitting Diodes through Inter-Dot Spacing Control. *Nat. Nanotechnol.* **2012**, *7*, 369–373.
9. Sonia, B.; Kelley, R.; Jelena, V. Engineered Quantum Dot Single-Photon Sources. *Rep. Prog. Phys.* **2012**, *75*, 126503.

10. Hyun, B.-R.; Choi, J. J.; Seyler, K. L.; Hanrath, T.; Wise, F. W. Heterojunction PbS Nanocrystal Solar Cells with Oxide Charge-Transport Layers. *ACS Nano* **2013**, *7*, 10938–10947.
11. Kramer, I. J.; Sargent, E. H. Colloidal Quantum Dot Photovoltaics: A Path Forward. *ACS Nano* **2011**, *5*, 8506–8514.
12. Ma, W.; Luther, J. M.; Zheng, H.; Wu, Y.; Alivisatos, A. P. Photovoltaic Devices Employing Ternary PbS_xSe_{1-x} Nanocrystals. *Nano Lett.* **2009**, *9*, 1699–1703.
13. Chuang, C.-H. M.; Brown, P. R.; Bulović, V.; Bawendi, M. G. Improved Performance and Stability in Quantum Dot Solar Cells through Band Alignment Engineering. *Nat. Mater.* **2014**, *13*, 796–801.
14. Schaller, R. D.; Klimov, V. I. High Efficiency Carrier Multiplication in PbSe Nanocrystals: Implications for Solar Energy Conversion. *Phys. Rev. Lett.* **2004**, *92*, 186601.
15. McGuire, J. A.; Joo, J.; Pietryga, J. M.; Schaller, R. D.; Klimov, V. I. New Aspects of Carrier Multiplication in Semiconductor Nanocrystals. *Acc. Chem. Res.* **2008**, *41*, 1810–1819.
16. Semonin, O. E.; Luther, J. M.; Choi, S.; Chen, H.-Y.; Gao, J.; Nozik, A. J.; Beard, M. C. Peak External Photocurrent Quantum Efficiency Exceeding 100% *via* MEG in a Quantum Dot Solar Cell. *Science* **2011**, *334*, 1530–1533.
17. Murray, C. B.; Sun, S.; Gaschler, W.; Doyle, H.; Betley, T. A.; Kagan, C. R. Colloidal Synthesis of Nanocrystals and Nanocrystal Superlattices. *IBM J. Res. Dev.* **2001**, *45*, 47–56.
18. Wehrenberg, B. L.; Wang, C.; Guyot-Sionnest, P. Interband and Intraband Optical Studies of PbSe Colloidal Quantum Dots. *J. Phys. Chem. B* **2002**, *106*, 10634–10640.
19. Lu, X.; Ziegler, K. J.; Ghezelbash, A.; Johnston, K. P.; Korgel, B. A. Synthesis of Germanium Nanocrystals in High Temperature Supercritical Fluid Solvents. *Nano Lett.* **2004**, *4*, 969–974.
20. Lee, D. C.; Pietryga, J. M.; Robel, I.; Werder, D. J.; Schaller, R. D.; Klimov, V. I. Colloidal Synthesis of Infrared-Emitting Germanium Nanocrystals. *J. Am. Chem. Soc.* **2009**, *131*, 3436–3437.
21. Keuleyan, S.; Lhuillier, E.; Guyot-Sionnest, P. Synthesis of Colloidal HgTe Quantum Dots for Narrow Mid-IR Emission and Detection. *J. Am. Chem. Soc.* **2011**, *133*, 16422–16424.
22. Rogach, A.; Kershaw, S. V.; Burt, M.; Harrison, M. T.; Kornowski, A.; Eychmüller, A.; Weller, H. Colloidally Prepared HgTe Nanocrystals with Strong Room-Temperature Infrared Luminescence. *Adv. Mater.* **1999**, *11*, 552–555.
23. Bennett, B. R.; Magno, R.; Shanabrook, B. V. Molecular Beam Epitaxial Growth of InSb, GaSb, and AlSb Nanometer-Scale Dots on GaAs. *Appl. Phys. Lett.* **1996**, *68*, 505–505.
24. Krier, A.; Huang, X. L.; Hammiche, A. Liquid Phase Epitaxial Growth and Morphology of InSb Quantum Dots. *J. Phys. D* **2001**, *34*, 874–878.
25. Shusterman, S.; Paltiel, Y.; Sher, A.; Ezersky, V.; Rosenwaks, Y. High-Density Nanometer-Scale InSb Dots Formation Using Droplets Heteroepitaxial Growth by Movpe. *J. Cryst. Growth* **2006**, *291*, 363–369.
26. Alphandéry, E.; Nicholas, R.; Mason, N.; Lyapin, S.; Klipstein, P. Photoluminescence of Self-Assembled InSb Quantum Dots Grown on GaSb as a Function of Excitation Power, Temperature, and Magnetic Field. *Phys. Rev. B* **2002**, *65*, 115322–115322.
27. Pryor, C.; Pistol, M. E. Band-Edge Diagrams for Strained III−V Semiconductor Quantum Wells, Wires, and Dots. *Phys. Rev. B* **2005**, *72*, 205311–205311.
28. Liu, W.; Chang, A. Y.; Schaller, R. D.; Talapin, D. V. Colloidal InSb Nanocrystals. *J. Am. Chem. Soc.* **2012**, *134*, 20258–20261.
29. Yarema, M.; Kovalenko, M. V. Colloidal Synthesis of InSb Nanocrystals with Controlled Polymorphism Using Indium and Antimony Amides. *Chem. Mater.* **2013**, *25*, 1788–1792.
30. Maurice, A.; Lopez Haro, M.; Hyot, B.; Reiss, P. Synthesis of Colloidal Indium Antimonide Nanocrystals Using Stibine. *Part. Part. Syst. Char.* **2013**, *30*, 828–831.
31. Adachi, S. *Properties of Group-IV, III-V, and II-VI Semiconductors*; John Wiley & Sons: New York, 2005; pp 147−172.
32. Wise, F. W. Lead Salt Quantum Dots: The Limit of Strong Quantum Confinement. *Acc. Chem. Res.* **2000**, *33*, 773–780.
33. Yoffe, A. D. Advances in Physics Low-Dimensional Systems: Quantum Size Effects and Electronic Properties of Semiconductor Microcrystallites (Zero-Dimensional Systems) and Some Quasi-Two-Dimensional Systems. *Adv. Phys.* **1993**, *42*, 173–266.
34. Luo, J.-W.; Franceschetti, A.; Zunger, A. Carrier Multiplication in Semiconductor Nanocrystals: Theoretical Screening of Candidate Materials Based on Band-Structure Effects. *Nano Lett.* **2008**, *8*, 3174–3181.
35. Efros, A. L.; Kharchenko, V. A.; Rosen, M. Breaking the Phonon Bottleneck in Nanometer Quantum Dots: Role of Auger-like Processes. *Solid State Commun.* **1995**, *93*, 281–284.
36. Guyot-Sionnest, P.; Shim, M.; Matranga, C.; Hines, M. Intraband Relaxation in CdSe Quantum Dots. *Phys. Rev. B* **1999**, *60*, R2181–R2184.
37. Klimov, V. I.; McBranch, D. W. Femtosecond 1p-to-1s Electron Relaxation in Strongly Confined Semiconductor Nanocrystals. *Phys. Rev. Lett.* **1998**, *80*, 4028–4031.
38. Schaller, R. D.; Pietryga, J. M.; Goupalov, S. V.; Petruska, M. A.; Ivanov, S. A.; Klimov, V. I. Breaking the Phonon Bottleneck in Semiconductor Nanocrystals *via* Multiphonon Emission Induced by Intrinsic Nonadiabatic Interactions. *Phys. Rev. Lett.* **2005**, *95*, 196401.
39. Schaller, R. D.; Pietryga, J. M.; Klimov, V. I. Carrier Multiplication in InAs Nanocrystal Quantum Dots with an Onset Defined by the Energy Conservation Limit. *Nano Lett.* **2007**, *7*, 3469–3476.
40. Achermann, M.; Petruska, M. A.; Crooker, S. A.; Klimov, V. I. Picosecond Energy Transfer in Quantum Dot Langmuir−Blodgett Nanoassemblies. *J. Phys. Chem. B* **2003**, *107*, 13782–13787.
41. Efros, A. L.; Rosen, M. Quantum Size Level Structure of Narrow-Gap Semiconductor Nanocrystals: Effect of Band Coupling. *Phys. Rev. B* **1998**, *58*, 7120–7135.
42. Klimov, V. I. Optical Nonlinearities and Ultrafast Carrier Dynamics in Semiconductor Nanocrystals. *J. Phys. Chem. B* **2000**, *104*, 6112–6123.
43. Garcia-Santamaria, F.; Chen, Y.; Vela, J.; Schaller, R. D.; Hollingsworth, J. A.; Klimov, V. I. Suppressed Auger Recombination in "Giant" Nanocrystals Boosts Optical Gain Performance. *Nano Lett.* **2009**, *9*, 3482–3488.
44. Leatherdale, C. A.; Woo, W. K.; Mikulec, F. V.; Bawendi, M. G. On the Absorption Cross Section of CdSe Nanocrystal Quantum Dots. *J. Phys. Chem. B* **2002**, *106*, 7619–7622.
45. Adachi, S. *Optical Constants of Crystalline and Amorphous Semiconductors: Numerical Data and Graphical Information*; Kluwer Academic Publishers: Norwell, MA, 1999.
46. Klimov, V. I.; McGuire, J. A.; Schaller, R. D.; Rupasov, V. I. Scaling of Multiexciton Lifetimes in Semiconductor Nanocrystals. *Phys. Rev. B* **2008**, *77*, 195324.
47. Robel, I.; Gresback, R.; Kortshagen, U.; Schaller, R. D.; Klimov, V. I. Universal Size-Dependent Trend in Auger Recombination in Direct-Gap and Indirect-Gap Semiconductor Nanocrystals. *Phys. Rev. Lett.* **2009**, *102*, 177404.
48. Schaller, R. D.; Petruska, M. A.; Klimov, V. I. Tunable Near-Infrared Optical Gain and Amplified Spontaneous Emission Using PbSe Nanocrystals. *J. Phys. Chem. B* **2003**, *107*, 13765–13768.
49. Guzelian, A. A.; Banin, U.; Kadavanich, A. V.; Peng, X.; Alivisatos, A. P. Colloidal Chemical Synthesis and Characterization of InAs Nanocrystal Quantum Dots. *Appl. Phys. Lett.* **1996**, *69*, 1432–1432.